



A Comparison of Cahn–Hilliard and Navier–Stokes–Cahn–Hilliard Models on Manifolds

Maxim Olshanskii¹ · Yerbol Palzhanov¹ · Annalisa Quaini¹ 

Received: 28 October 2021 / Accepted: 18 February 2022

© Vietnam Academy of Science and Technology (VAST) and Springer Nature Singapore Pte Ltd. 2022

Abstract

We consider phase-field models with and without lateral flow for the numerical simulation of lateral phase separation and coarsening in lipid membranes. For the numerical solution of these models, we apply an unfitted finite element method that is flexible in handling complex and possibly evolving shapes in the absence of an explicit surface parametrization. Through several numerical tests, we investigate the effect of the presence of lateral flow on the evolution of phases. In particular, we focus on understanding how variable line tension, viscosity, membrane composition, and surface shape affect the pattern formation.

Keywords Lateral phase separation · Surface Cahn–Hilliard equation · Lateral flow · Surface Navier–Stokes–Cahn–Hilliard system · TraceFEM

Mathematics Subject Classification (2010) 65N30 · 76D05 · 76T99

1 Introduction

Recent years have witnessed an increased interest in studying phase separation in biological membranes [9, 31]. This is due to the fact that lateral phase separation has been recognized as a critical mechanism for dynamic control of the spatial organization of membrane components [26, 36]. The lipid bilayer in biological membranes may be organized into one of two phases: liquid disordered and liquid ordered [5]. The liquid ordered domains, also

Dedicated to Prof. Alfio Quarteroni on the occasion of his 70th birthday.

✉ Annalisa Quaini
aquaini@uh.edu

Maxim Olshanskii
maolshanskiy@uh.edu

Yerbol Palzhanov
ypalzhanov@uh.edu

¹ Department of Mathematics, University of Houston, 3551 Cullen Blvd, Houston, TX, 77204, USA

known as lipid rafts, have been linked to a wide range of cellular functions, from membrane trafficking to inter- and intracellular signaling [22]. In addition, domain formation on membranes has also been utilized to create novel membrane-based materials with heterogeneous surfaces [6, 43].

Phase separation and pattern formation in lipid bilayers has been studied theoretically (see, e.g., [4, 21, 27, 42]), experimentally (see, e.g., [8, 49]), and numerically (see, e.g., [17, 30, 32–34, 37, 46, 50]). Computational studies are particularly useful to observe the dynamics of phases, which is hard to address theoretically, and to gain insights that are too expensive (or even impossible) to obtain experimentally. In this paper, we choose a continuum-based computational approach that relies on a phase-field description. In such approach, a smooth indicator function is used to distinguish between ordered and disordered phases of a matter; see [10, 11, 23, 48] for an introduction to the topic. Emerged as a powerful computational approach to modeling and predicting phase separation in materials and fluids, the phase-field method describes the system using a set of field variables that are continuous across the interfacial regions separating the phases.

In our previous work, we have developed a computationally efficient method based on the surface Cahn–Hilliard (CH) phase-field model to predict the phase behavior and domain formation on heterogeneous membranes [52, 53]. More recently, such method has been validated against laboratory experiments [54]. While a good agreement was achieved between numerical results and experimental data, the CH model does not account for viscous and fluidic phenomena that are recognized to be important in lipid membranes [28]. In fact, it has been demonstrated that membrane fluidity within the liquid ordered domains can be substantially lower than that in the liquid disordered phase [44], affecting the coarsening dynamics of rafts on membranes [47]. In order to capture these phenomena, in [41] we have considered the more complex surface Navier–Stokes–Cahn–Hilliard (NSCH) model and a numerical method for it.

Although the importance of viscous dissipation and fluidity in lipid membranes is acknowledged, it remains to be understood how lateral flow affects pattern formation. Thus, in this paper we compare the evolution of phases as predicted by the CH model (i.e., without lateral flow) and NSCH model (i.e., with lateral flow) through a series of numerical tests. For the numerical solution of both models, we apply an unfitted finite element method called the trace finite element method (TraceFEM) [38, 39]. See [14] for the review of other surface FEM. We opted for an unfitted finite element method because of its flexibility in handling complex shapes, as we will show in this paper, and possibly evolving surfaces, as shown in [53] for the CH model. For additional numerical studies on the evolving CH equation, we refer the reader to [15, 16]. Although the surfaces treated in this paper are steady, our interest in evolving surfaces is associated with our long term goal of simulating membrane-based drug carriers that used phase-separated patterns to facilitate fusion with the target cell [54]. Among all unfitted finite element methods, TraceFEM has several advantages that make it appealing: i) it employs a sharp surface representation, ii) surfaces can be defined implicitly and no surface parametrization is required, iii) the number of active degrees of freedom is asymptotically optimal, and iv) the order of convergence is optimal. An alternative to unfitted finite element methods is given by, e.g., Isogeometric Analysis [7, 12].

The paper outline is as follows. In Section 2, we state the two phase-field models and their variational formulations. The application of TraceFEM to both models is described in Section 3. In Section 4, we report several numerical results obtained with both models on the surface of a sphere and an asymmetric torus. Section 5 provides concluding remarks.

2 Mathematical Model

In order to formulate the surface the CH and NSCH equations, we need some notation. Let Γ be an arbitrary-shaped closed, smooth, and stationary surface, with the outward pointing unit normal \mathbf{n} . Let $\mathbf{P} = \mathbf{P}(\mathbf{x}) := \mathbf{I} - \mathbf{n}(\mathbf{x})\mathbf{n}(\mathbf{x})^T$ for $\mathbf{x} \in \Gamma$ be the orthogonal projection onto the tangent plane. For a scalar function $p : \Gamma \rightarrow \mathbb{R}$ or a vector function $\mathbf{u} : \Gamma \rightarrow \mathbb{R}^3$ we define $p^e : \mathcal{O}(\Gamma) \rightarrow \mathbb{R}$, $\mathbf{u}^e : \mathcal{O}(\Gamma) \rightarrow \mathbb{R}^3$ as suitable extensions of p and \mathbf{u} from Γ to its neighborhood $\mathcal{O}(\Gamma)$. The surface gradient and covariant derivatives on Γ are then defined as $\nabla_\Gamma p = \mathbf{P}\nabla p^e$ and $\nabla_\Gamma \mathbf{u} := \mathbf{P}\nabla \mathbf{u}^e \mathbf{P}$. These definitions are independent of a particular smooth extension of p and \mathbf{u} off Γ . On Γ we consider the surface rate-of-strain tensor [20] given by

$$E_s(\mathbf{u}) := \frac{1}{2}(\nabla_\Gamma \mathbf{u} + (\nabla_\Gamma \mathbf{u})^T).$$

The surface divergence operators for a vector $\mathbf{g} : \Gamma \rightarrow \mathbb{R}^3$ and a tensor $\mathbf{A} : \Gamma \rightarrow \mathbb{R}^{3 \times 3}$ are defined as:

$$\operatorname{div}_\Gamma \mathbf{g} := \operatorname{tr}(\nabla_\Gamma \mathbf{g}), \quad \operatorname{div}_\Gamma \mathbf{A} := \left(\operatorname{div}_\Gamma (\mathbf{e}_1^T \mathbf{A}), \operatorname{div}_\Gamma (\mathbf{e}_2^T \mathbf{A}), \operatorname{div}_\Gamma (\mathbf{e}_3^T \mathbf{A}) \right)^T,$$

with \mathbf{e}_i the i th standard basis vector in \mathbb{R}^3 and $\operatorname{tr}(\cdot)$ is the trace of a matrix. The Laplace–Beltrami operator for a sufficiently smooth function g in a neighborhood of Γ is:

$$\Delta_\Gamma g := \operatorname{div}_\Gamma (\nabla_\Gamma g).$$

Further $L^2(\Gamma)$ is the Lebesgue space of square-integrable functions on Γ and $H^1(\Gamma)$ is the Sobolev space of all functions $g \in L^2(\Gamma)$ such that $\nabla_\Gamma g \in L^2(\Gamma)^3$.

On Γ we consider a heterogeneous mixture of two species with surface fractions $c_i = S_i/S$, $i = 1, 2$, where S_i are the surface area occupied by the components and S is the surface area of Γ . Since $S = S_1 + S_2$, we have $c_1 + c_2 = 1$. Let c_1 be the representative surface fraction, i.e. $c = c_1$.

2.1 The Cahn–Hilliard Problem

A well established model for the process of spinodal decomposition and phase separation alone (i.e., in the absence of surface fluid flow) is the CH phase-field model [10, 11]. The surface CH equation governs the evolution in time t of $c = c(t, \mathbf{x})$, $\mathbf{x} \in \Gamma \subset \mathbb{R}^3$:

$$\frac{\partial c}{\partial t} = \operatorname{div}_\Gamma \left(M \nabla_\Gamma \left(\frac{1}{\epsilon} f_0'(c) - \epsilon \Delta_\Gamma c \right) \right) \quad \text{on } \Gamma, \text{ for } t \in (0, T], \tag{1}$$

suitably endowed with an initial condition $c(0, \mathbf{x}) = c_0$. In (1), $f_0(c) = \frac{1}{4} c^2 (1 - c)^2$ is the specific free energy of a homogeneous phase, parameter $\epsilon > 0$ defines the width of the (diffuse) interface between the phases, M is the so-called mobility (see [29]), and T is the end of a time interval of interest. We note that the above f_0 is a smooth approximation of the physically relevant potential [10, 11]. We consider the degenerate mobility of the form

$$M = Dc(1 - c) \tag{2}$$

with diffusivity constant $D > 0$. Mobility (2) is a popular choice for numerical studies. Equation (1) is obtained from minimizing the total specific free energy $\int_\Gamma \frac{1}{\epsilon} f_0(c) + \frac{1}{2} \epsilon |\nabla_\Gamma c|^2 ds$ subject to the conservation of surface area $\int_\Gamma c ds$.

Equation (1) is a fourth-order equation. In order to avoid higher order spatial derivatives, which would need careful numerical treatment, it is common to rewrite (1) as two coupled

second-order equations:

$$\frac{\partial c}{\partial t} = \operatorname{div}_\Gamma (M \nabla_\Gamma \mu) \quad \text{on } \Gamma, \tag{3}$$

$$\mu = \frac{1}{\epsilon} f'_0 - \epsilon \Delta_\Gamma c \quad \text{on } \Gamma. \tag{4}$$

In (4), μ represents the chemical potential.

For the numerical method, we need a weak (integral) formulation. In order to devise it, one multiplies (3) by $v \in H^1(\Gamma)$ and (4) by $q \in H^1(\Gamma)$, integrates over Γ and employs the integration by parts identity. The weak (variational) formulation of problem (3)–(4) reads: Find $(c, \mu) \in H^1(\Gamma) \times H^1(\Gamma)$ such that

$$\int_\Gamma \frac{\partial c}{\partial t} v \, ds + \int_\Gamma M \nabla_\Gamma \mu \nabla_\Gamma v \, ds = 0, \tag{5}$$

$$\int_\Gamma \mu q \, ds - \int_\Gamma \frac{1}{\epsilon} f'_0(c) q \, ds - \int_\Gamma \epsilon \nabla_\Gamma c \nabla_\Gamma q \, ds = 0, \tag{6}$$

for all $(v, q) \in H^1(\Gamma) \times H^1(\Gamma)$.

2.2 The Navier–Stokes–Cahn–Hilliard Problem

Let us now consider the case of phase separation occurring together with lateral flow. The classical phase-field model for the flow of two immiscible, incompressible, and Newtonian fluids with the same density is the so-called *Model H* [24]. To be able to account for non-matching densities, here we focus on a generalization of Model H first presented in [41], which builds on the thermodynamically consistent model introduced in [1].

To state the NSCH model, let m_i be the mass of component i and m is the total mass. The density of the mixture can be expressed as $\rho = \frac{m}{S} = \frac{m_1}{S_1} \frac{S_1}{S} + \frac{m_2}{S_2} \frac{S_2}{S}$. Thus, $\rho = \rho(c) = \rho_1 c + \rho_2(1 - c)$ for $c \in [0, 1]$, where densities $\rho_1, \rho_2 > 0$ are given constants. Similarly, for the dynamic viscosity of the mixture we can write $\eta = \eta(c) = \eta_1 c + \eta_2(1 - c)$ for $c \in [0, 1]$, where $\eta_1, \eta_2 > 0$ are the constant dynamic viscosities of the two species. Since the polynomial double-well potential $f_0(c)$ does not enforce $c \in [0, 1]$, we use a smooth cut-off function to ensure $\rho(c) \geq \rho_{\min} > 0$, $\eta(c) \geq \eta_{\min} > 0$, while preserving the linear dependence for $c > 0$ [41]. Then, the governing equations read:

$$\rho \partial_t \mathbf{u} + \rho (\nabla_\Gamma \mathbf{u}) \mathbf{u} - \mathbf{P} \operatorname{div}_\Gamma (2\eta E_s(\mathbf{u})) + \nabla_\Gamma p = -\sigma_\gamma c \nabla_\Gamma \mu + M \theta (\nabla_\Gamma (\theta \mathbf{u})) \nabla_\Gamma \mu, \tag{7}$$

$$\operatorname{div}_\Gamma \mathbf{u} = 0, \tag{8}$$

$$\partial_t c + \operatorname{div}_\Gamma (c \mathbf{u}) - \operatorname{div}_\Gamma (M \nabla_\Gamma \mu) = 0, \tag{9}$$

$$\mu = \frac{1}{\epsilon} f'_0 - \epsilon \Delta_\Gamma c, \tag{10}$$

on $\Gamma \times (0, T]$. Here, \mathbf{u} is the surface averaged tangential velocity, p is pressure, σ_γ is line tension, and $\theta^2 = \frac{d\rho}{dc}$. All other variables and parameters are the same as defined in Section 2.1. Without loss of generality we let $\rho_1 \geq \rho_2$. Then, the model (7)–(10) assumes that ρ is a smooth monotonic function of c , i.e. $\frac{d\rho}{dc} \geq 0$. We note that system (7)–(10) coincides with the model in [1] in the range of linear ρ – c dependence, but it exhibits thermodynamic consistency for a general monotone ρ – c relation. See [41] for details. The energy

balance delivered by the model reads [41]:

$$\begin{aligned} \frac{d}{dt} \int_{\Gamma} \left(\frac{\rho}{2} |\mathbf{u}|^2 + \sigma_{\gamma} \left(\frac{1}{\epsilon} f_0 + \frac{\epsilon}{2} |\nabla_{\Gamma} c|^2 \right) \right) ds \\ + \int_{\Gamma} 2\eta |E_s(\mathbf{u})|^2 ds + \int_{\Gamma} \sigma_{\gamma} M |\nabla_{\Gamma} \mu|^2 ds = 0. \end{aligned} \tag{11}$$

The only difference between model (7)–(10) and Model H is the last term in (7), which can be interpreted as an additional momentum flux due to diffusion of the components driven by the gradient of the chemical potential. This term vanishes for matching densities since $\theta = \sqrt{\frac{d\rho}{dc}} = 0$, thereby recovering Model H. For other thermodynamic consistent extensions of Model H that involve a generic smooth $\rho(c)$ (no monotonicity assumption), the reader is referred to [2, 3].

For the purpose of writing the weak formulation of problem (7)–(10), we define the spaces

$$\mathbf{V}_T := \{ \mathbf{u} \in H^1(\Gamma)^3 \mid \mathbf{u} \cdot \mathbf{n} = 0 \}, \quad L_0^2(\Gamma) := \left\{ p \in L^2(\Gamma) \mid \int_{\Gamma} p \, ds = 0 \right\}.$$

The weak formulation of the surface NSCH problem (7)–(10) reads: Find $(\mathbf{u}, p, c, \mu) \in \mathbf{V}_T \times L_0^2(\Gamma) \times H^1(\Gamma) \times H^1(\Gamma)$ such that

$$\begin{aligned} \int_{\Gamma} (\rho \partial_t \mathbf{u} \cdot \mathbf{v} + \rho (\nabla_{\Gamma} \mathbf{u}) \mathbf{u} \cdot \mathbf{v} + 2\eta E_s(\mathbf{u}) : E_s(\mathbf{v})) \, ds - \int_{\Gamma} p \operatorname{div}_{\Gamma} \mathbf{v} \, ds \\ = - \int_{\Gamma} \sigma_{\gamma} c \nabla_{\Gamma} \mu \cdot \mathbf{v} \, ds + \int_{\Gamma} M (\nabla_{\Gamma}(\theta \mathbf{u})) (\nabla_{\Gamma} \mu) \cdot (\theta \mathbf{v}) \, ds, \end{aligned} \tag{12}$$

$$\int_{\Gamma} q \operatorname{div}_{\Gamma} \mathbf{u} \, ds = 0, \tag{13}$$

$$\int_{\Gamma} \partial_t c \, v \, ds - \int_{\Gamma} \mathbf{c} \mathbf{u} \cdot \nabla_{\Gamma} v \, ds + \int_{\Gamma} M \nabla_{\Gamma} \mu \cdot \nabla_{\Gamma} v \, ds = 0, \tag{14}$$

$$\int_{\Gamma} \mu \, g \, ds = \int_{\Gamma} \frac{1}{\epsilon} f_0'(c) \, g \, ds + \int_{\Gamma} \epsilon \nabla_{\Gamma} c \cdot \nabla_{\Gamma} g \, ds, \tag{15}$$

for all $(\mathbf{v}, q, v, g) \in \mathbf{V}_T \times L^2(\Gamma) \times H^1(\Gamma) \times H^1(\Gamma)$. More details on the derivation of (12)–(15) can be found in [41].

3 Numerical Method

For the numerical solution of the problems presented in Section 2, we apply the trace finite element method (TraceFEM) [38, 39]. TraceFEM relies on a tessellation of a 3D bulk computational domain Ω ($\Gamma \subset \Omega$ holds) into shape-regular tetrahedra untangled to the position of Γ .

Surface Γ is defined as the zero level set of a function ϕ (where ϕ is at least Lipschitz continuous), i.e. $\Gamma = \{ \mathbf{x} \in \Omega : \phi(\mathbf{x}) = 0 \}$, such that $|\nabla \phi| \geq c_0 > 0$ in a 3D neighborhood $U(\Gamma)$ of the surface. The vector field $\mathbf{n} = \nabla \phi / |\nabla \phi|$ is normal on Γ and defines quasi-normal directions in $U(\Gamma)$. Let \mathcal{T}_h be the collection of all tetrahedra such that $\overline{\Omega} = \cup_{T \in \mathcal{T}_h} \overline{T}$, with h denoting the characteristic tetrahedra size. The subset of tetrahedra that have a nonzero intersection with Γ is denoted by \mathcal{T}_h^{Γ} . We allow for local refinement of the grid towards Γ . The domain formed by all tetrahedra in \mathcal{T}_h^{Γ} is denoted by Ω_h^{Γ} .

In order to state the fully discretized CH and NSCH problems, we introduce some finite element spaces. Let V_h^k denote the bulk (volumetric) finite element space of continuous functions that are polynomials of degree k on each $T \in \mathcal{T}_h^\Gamma$:

$$V_h^k = \{v \in C(\Omega_h^\Gamma) : v \in P_k(T) \text{ for any } T \in \mathcal{T}_h^\Gamma\}.$$

The traces of functions from V_h^1 on Γ will be used to approximate the surface fraction and the chemical potential. Our bulk velocity and pressure finite element spaces are the Taylor–Hood elements on Ω_h^Γ :

$$\mathbf{V}_h = (V_h^2)^3, \quad Q_h = V_h^1 \cap L_0^2(\Gamma). \tag{16}$$

Higher order approximations are possible (see, e.g., [19, 41]) but will not be considered here.

For the purpose of numerical integration, we approximate Γ by a “discrete” surface Γ_h so that integrals over Γ_h can be computed accurately and efficiently. For first order finite elements, a straightforward polygonal approximation of Γ ensures that the geometric approximation error is consistent with the finite element interpolation error. See, e.g., [38].

Next, we introduce two finite element bilinear forms that are common to the discrete versions of both NS and NSCH problems:

$$a_\mu(\mu, v) := \int_\Gamma M \nabla_\Gamma \mu \cdot \nabla_\Gamma v \, ds + \tau_\mu \int_{\Omega_h^\Gamma} (\mathbf{n} \cdot \nabla \mu)(\mathbf{n} \cdot \nabla v) \, d\mathbf{x}, \tag{17}$$

$$a_c(c, g) := \epsilon \int_\Gamma \nabla_\Gamma c \cdot \nabla_\Gamma g \, ds + \tau_c \int_{\Omega_h^\Gamma} (\mathbf{n} \cdot \nabla c)(\mathbf{n} \cdot \nabla g) \, d\mathbf{x}. \tag{18}$$

Forms (17)–(18) are well defined for $\mu, v, c, g \in H^1(\Omega_h^\Gamma)$. The volumetric terms in (17) and (18) are there to recover algebraic stability as possible small cuts of tetrahedra from \mathcal{T}_h^Γ by Γ may lead to poorly conditioned algebraic systems. Notice that these terms are consistent up to geometric errors related to the approximation of Γ by Γ_h and \mathbf{n} by \mathbf{n}_h . We set the stabilization parameters as follows [52]: $\tau_\mu = h, \tau_c = \epsilon h^{-1}$.

For the time discretization, let $\Delta t = \frac{T}{N}$ be a time step. For ease of presentation, the time step is assumed to be fixed, although adaptive time stepping techniques can be applied [18]. At time instance $t^n = n\Delta t$, ζ^n denotes the approximation of generic variable $\zeta(t^n, \mathbf{x})$. To approximate the time derivatives in problems (5)–(6) and (12)–(15), we use the backward differentiation formula of order 1:

$$[\zeta]_t^n = \frac{\zeta^n - \zeta^{n-1}}{\Delta t}.$$

Once fully discretized, CH problem (5)–(6) reads: Given $c_h^n \in V_h^1$, find $(c_h^{n+1}, \mu_h^{n+1}) \in V_h^1 \times V_h^1$ such that:

$$\begin{aligned} ([c_h]_t^{n+1}, v_h) + a_\mu(\mu_h^{n+1}, v_h) &= 0, \\ \left(\mu_h^{n+1} - \frac{\gamma c \Delta t}{\epsilon} [c_h]_t^{n+1} - \frac{1}{\epsilon} f_0'(c_h^n), g_h \right) - a_c(c_h^{n+1}, g_h) &= 0, \end{aligned} \tag{19}$$

for all $(v_h, g_h) \in V_h^1 \times V_h^1$. Following [45], the second term in (19) stabilizes the explicit treatment of non-linear part of the free energy variation.

Next, we turn to the NSCH problem (12)–(15). For its numerical solution, we adopt a decoupled linear finite element method introduced in [41]. In order to described such method, we need to introduce some additional forms related to the Navier–Stokes part of

the problem and the decomposition of a vector field on Γ into its tangential and normal components: $\mathbf{u} = \bar{\mathbf{u}} + (\mathbf{u} \cdot \mathbf{n})\mathbf{n}$. The additional forms are defined as follows:

$$a(\eta; \mathbf{u}, \mathbf{v}) := \int_{\Gamma} 2\eta E_s(\bar{\mathbf{u}}) : E_s(\bar{\mathbf{v}}) ds + \tau \int_{\Gamma} (\mathbf{n} \cdot \mathbf{u})(\mathbf{n} \cdot \mathbf{v}) ds + \beta_u \int_{\Omega_h^{\Gamma}} [(\mathbf{n} \cdot \nabla)\mathbf{u}] \cdot [(\mathbf{n} \cdot \nabla)\mathbf{v}] + \hat{\gamma} \int_{\Gamma} \operatorname{div}_{\Gamma} \mathbf{u} \operatorname{div}_{\Gamma} \mathbf{v} ds d\mathbf{x}, \tag{20}$$

$$c(\rho; \mathbf{w}, \mathbf{u}, \mathbf{v}) := \int_{\Gamma} \rho \mathbf{v}^T (\nabla_{\Gamma} \bar{\mathbf{u}}) \mathbf{w} ds + \frac{1}{2} \int_{\Gamma} \hat{\rho} (\operatorname{div}_{\Gamma} \bar{\mathbf{w}}) \bar{\mathbf{u}} \cdot \bar{\mathbf{v}} ds, \tag{21}$$

$$b(\mathbf{u}, q) := \int_{\Gamma} \mathbf{u} \cdot \nabla_{\Gamma} q ds, \tag{22}$$

$$s(p, q) := \beta_p \int_{\Omega_h^{\Gamma}} \nabla p \cdot \nabla q d\mathbf{x}, \tag{23}$$

where $\hat{\gamma}$ is the grad-div stabilization parameter [40] (set equal to 1) and $\hat{\rho} = \rho - \frac{d\rho}{dc}c$. Forms (20)–(23) are well defined for $p, q \in H^1(\Omega_h^{\Gamma}) \cap H^1(\Gamma)$, $\mathbf{u}, \mathbf{v}, \mathbf{w} \in H^1(\Omega_h^{\Gamma})^3 \cap H^1(\Gamma)^3$. In (20), $\tau > 0$ is a penalty parameter to enforce the tangential constraint (i.e., condition $\mathbf{u}_h \cdot \mathbf{n} = 0$ on Γ for $\mathbf{u}_h \in \mathbf{V}_h$), while $\beta_u \geq 0$ in (20) and $\beta_p \geq 0$ in (23) are stabilization parameters to deal with possible small cuts. They are set according to [25]: $\tau = h^{-2}$, $\beta_p = h$, $\beta_u = h^{-1}$.

The decoupled finite element method from [41] requires the solution of one linear problem Cahn–Hilliard type system (step 1) and one linearized Navier–Stokes system (step 2) per time step t^{n+1} , thereby ensuring low computational costs. This scheme reads:

- Step 1: Given $\mathbf{u}_h^n \in \mathbf{V}_h$ and $c_h^n \in V_h^1$, find $(c_h^{n+1}, \mu_h^{n+1}) \in V_h^1 \times V_h^1$ such that:

$$\begin{aligned} & \left([c_h]_t^{n+1}, v_h \right) - \left(\mathbf{u}_h^n c_h^{n+1}, \nabla_{\Gamma} v_h \right) + a_{\mu}(\mu_h^{n+1}, v_h) = 0, \\ & \left(\mu_h^{n+1} - \frac{\gamma c \Delta t}{\epsilon} [c_h]_t^{n+1} - \frac{1}{\epsilon} f'_0(c_h^n), g_h \right) - a_c(c_h^{n+1}, g_h) = 0, \end{aligned}$$

for all $(v_h, g_h) \in V_h^1 \times V_h^1$.

- Step 2: Set $\theta^{n+1} = \sqrt{\frac{d\rho}{dc}(c_h^{n+1})}$. Find $(\mathbf{u}_h^{n+1}, p_h^{n+1}) \in \mathbf{V}_h \times Q_h$ such that

$$\begin{aligned} & \left(\rho^n [\bar{\mathbf{u}}_h]_t^{n+1}, \mathbf{v}_h \right) + c \left(\rho^{n+1}; \mathbf{u}_h^n, \mathbf{u}_h^{n+1}, \mathbf{v}_h \right) + a \left(\eta^{n+1}; \mathbf{u}_h^{n+1}, \mathbf{v}_h \right) + b \left(\mathbf{v}_h, p_h^{n+1} \right) \\ & = - \left(\sigma_{\gamma} c_h^{n+1} \nabla_{\Gamma} \mu_h^{n+1}, \mathbf{v}_h \right) + M \left((\nabla_{\Gamma}(\theta^{n+1} \bar{\mathbf{u}}_h^{n+1})) \nabla_{\Gamma} \mu_h^{n+1}, \theta^{n+1} \mathbf{v}_h \right) + \left(\mathbf{f}_h^{n+1}, \mathbf{v}_h \right), \\ & b \left(\mathbf{u}_h^{n+1}, q_h \right) - s \left(p_h^{n+1}, q_h \right) = 0 \end{aligned}$$

for all $(\mathbf{v}_h, q_h) \in \mathbf{V}_h \times Q_h$.

In [41, Theorem 4.2], we proved that the above scheme is stable under relatively mild restrictions on time-step and mesh size. However, in the numerical results presented in [41] and in Section 4 of this paper, we observed only a restriction of the form $h \lesssim \epsilon$, which is very typical for a phase field approach. Moreover, we note that failure to resolve the interface, i.e. $h \geq \epsilon$, leads to inaccurate computed solutions rather than a blow-up in time. We speculate that restrictions on h in terms of Δt in Theorem 4.2 of [41] may be an artifact of the analysis.

4 Numerical Results

We present a series of numerical results aimed at understanding the difference in the evolution of phases when modeled by the Cahn–Hilliard or Navier–Stokes–Cahn–Hilliard equations posed on a closed smooth surface. For the latter model, we experiment with different settings for the physical parameters. All the numerical results have been obtained with open source finite element package DROPS [13].

We start by comparing the numerical results produced by the two models on a sphere in Section 4.1. Then, we consider an asymmetric torus in Section 4.2 to see the effects of a different geometry on the evolution of phases. More complex shapes are treated in [52], where we performed a computational study of two phase separation models with no surface flow (surface Allen–Cahn and Cahn–Hilliard equations). For all the simulations we set $\epsilon = 0.02$ and $D = 0.02$ in (2). In order to model an initially homogenous mix of components, the initial area fraction c_0 is defined as a realization of Bernoulli random variable $c_{\text{rand}} \sim \text{Bernoulli}(a)$ with mean value a , i.e. we set:

$$c_0 := c_{\text{rand}}(\mathbf{x}) \quad \text{for active mesh nodes } \mathbf{x}. \quad (24)$$

We set $a = 0.5$ for the 50%-50% composition (meaning that 50% of the surface is covered by one phase and the remaining 50% by the other phase) and $a = 0.3$ for the 30%-70% composition. The other physical parameters will be specified for each case. We run all the simulations till $T = 100$ and with an adaptive time stepping technique [18].

For all the simulations, we will study the evolution of the discrete Lyapunov energy:

$$E_h^L(c_h) = \int_{\Gamma_h} f(c_h) ds = \int_{\Gamma_h} \left(\frac{1}{\epsilon} f_0(c_h) + \frac{1}{2} \epsilon |\nabla_{\Gamma} c_h|^2 \right) ds \quad (25)$$

and we will visually compare the evolutions of phases. In addition, for the NSCH model we will compare the flow in a qualitative way.

4.1 Phase Separation on a Sphere

The surface of the sphere is appealing for its simplicity and for its relevance in practical applications. In fact, lipid vesicles used as drug carriers have a spherical shape [54]. We characterize Γ as the zero level set of function $\phi(\mathbf{x}) = \|\mathbf{x}\|_2 - 1$ and we embed it in an outer cubic domain $\Omega = [-5/3, 5/3]^3$.

We experimented with different meshes to find one with an appropriate level of refinement for the given value of ϵ . The initial triangulation \mathcal{T}_{h_ℓ} of Ω we considered consists of eight sub-cubes, where each of the sub-cubes is further subdivided into six tetrahedra. We applied several level of refinement $\ell \in \mathbb{N}$, with associated mesh size $h_\ell = \frac{10/3}{2^{\ell+1}}$. Each mesh also features a refinement towards the surface. We found that $\ell = 5$ is a good compromise between accuracy and computational cost. See also [41]. Thus, the results reported in this section refer to the mesh with $\ell = 5$. We note that for the NSCH model such mesh has 225822 active degrees of freedom (193086 for \mathbf{u}_h and 10912 for p_h, c_h , and μ_h).

4.1.1 Variable Line Tension

In this section, we focus on composition 50%-50%. One initial condition (24) is generated and used to compare phase separation given by the CH model and the NSCH model with variable line tension. We assign density $\rho_1 = 3$ and viscosity $\eta_1 = 0.1$ to species 1, while species 2 has $\rho_2 = 1$ and $\eta_2 = 0.008$. We consider a low value of line tension $\sigma_\gamma = 0.004$

and one high value $\sigma_\gamma = 0.4$. These are dimensionless values that allow us to explore the interplay between different physical phenomena. For realistic values of the physical parameters in lipid vesicles, we refer to [51, 54].

Figure 1 shows the Lyapunov energy (25) over time computed by the CH model, NSCH model with low and high line tension. We observe that when switching from the CH model to NSCH model with low line tension the Lyapunov energy decay is slightly faster. It becomes substantially faster when the value of σ_γ is increased, which can be expected from the energy balance (11) since the last dissipative term scales with σ_γ .

These differences are reflected in the evolution of phases displayed in Fig. 2. The evolution of the surface fraction does not vary significantly when going from the CH model to the NSCH model with $\sigma_\gamma = 0.004$, although some differences can be noticed from $t = 30$ on. Changing to $\sigma_\gamma = 0.4$ produces more evident differences, starting already from $t = 5$. Moreover, by comparing the center and bottom rows in Fig. 2 it is clear that a larger value of σ_γ accelerates the transition towards a steady state, i.e. one large black domain and one large pink domain separated by a minimal length interface.

Figure 3 displays the velocity vectors superimposed to the surface fraction for the bottom two cases in Fig. 2. Since for visualization purposes the arrows have been magnified with different factors, the velocity vectors cannot be compared across rows. In the NSCH model in (7)–(10), the fluid flow is purely driven by the coupling with the phase separation process. For $\sigma_\gamma = 0.4$ (bottom row in Fig. 3), the larger surface tension forces initially produce more significant fluid motion, which however decays faster over time. This is due to the fact that the system evolves more rapidly towards a steady state, as mentioned above. This is not the case for $\sigma_\gamma = 0.004$. See Fig. 3, top row.

4.1.2 Variable Viscosity

Now, we set line tension to $\sigma_\gamma = 0.04$ and vary the viscosity for composition 50%-50% and 30%-70% (which means that 30% of the surface is in phase 1). We consider a high viscosity

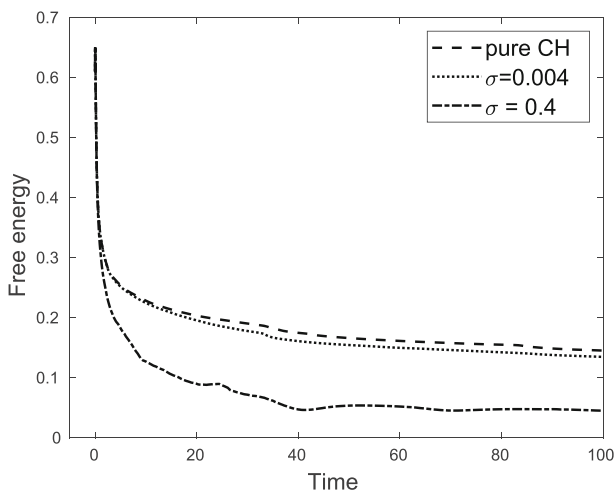


Fig. 1 Discrete Lyapunov energy (25) given by the CH model, NSCH model with $\sigma_\gamma = 0.004$, and NSCH model with $\sigma_\gamma = 0.4$

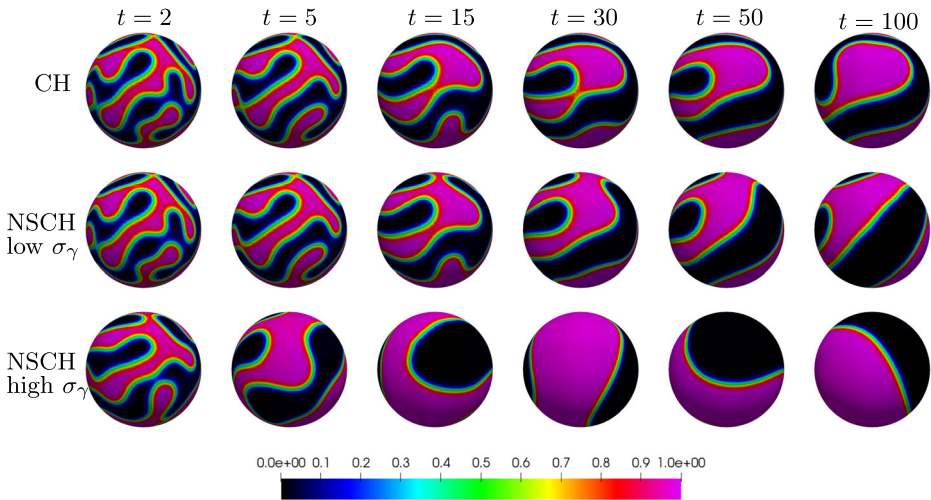


Fig. 2 Phase separation given by the CH model (top), NSCH model with $\sigma_\gamma = 0.004$ (center), and NSCH model with $\sigma_\gamma = 0.4$ (bottom)

case ($\eta_1 = 0.01$, $\eta_2 = 0.0008$) and a low viscosity case ($\eta_1 = 0.0001$, $\eta_2 = 0.000008$). The densities are set like in Section 4.1.1.

Figure 4 reports the discrete Lyapunov energy (25) over time computed by the CH model, NSCH model with low and high viscosities for both compositions. We observe that the presence of surface flow leads to a faster Lyapunov energy decay. In the case of composition 50%-50%, we see that switching from high to low values of the viscosity does not produce a significant change in the energy decay. Instead, for composition 30%-70% Fig. 4 shows that lower values of viscosity lead to a faster Lyapunov energy decay than higher values. An explanation of this phenomenon is not obvious from the energy balance (11), since the first dissipation term scales with viscosity. To ensure that this was not an accident, we repeated the numerical experiment for composition 30%-70% ten times with different realizations of initial condition (24). The average Lyapunov energy computed by CH model and NSCH model with low and high viscosities is reported in Fig. 5, which confirms the trend. It seems plausible to hypothesize the following: for lower viscosity the surface tension produces

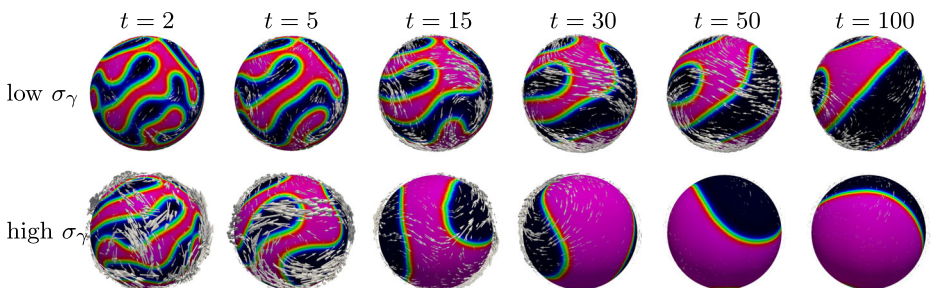


Fig. 3 Velocity vectors superimposed to the surface fraction for $\sigma_\gamma = 0.004$ (top) and $\sigma_\gamma = 0.4$ (bottom). For visualization purposes, the velocity vectors are magnified by a factor 40 in the top row and 2 in the bottom row

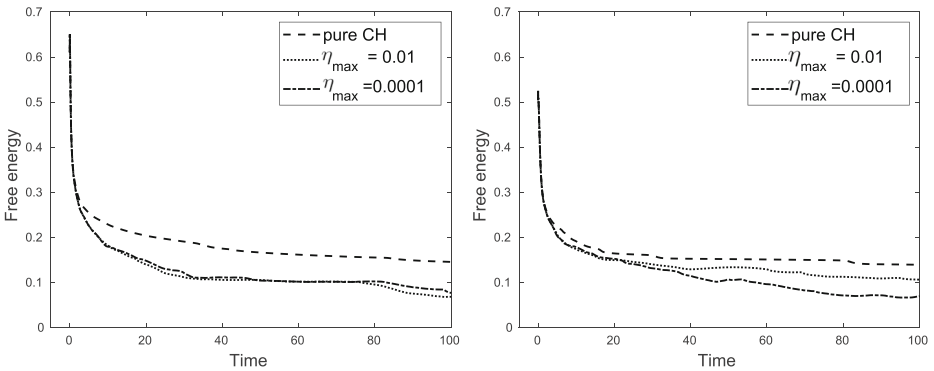


Fig. 4 Discrete Lyapunov energy (25) given by the CH model, NSCH model with high values of viscosities ($\eta_1 = 0.01$, $\eta_2 = 0.0008$), and NSCH model with low values of viscosities ($\eta_1 = 0.0001$, $\eta_2 = 0.000008$) for composition 50%-50% (left) and 30%-70% (right)

higher speed lateral flows (as illustrated in Fig. 3), which increases the probability of small rafts coming together and merging, thereby releasing the free energy.

Figures 6 and 7 show the evolution of phase separation by the CH model and NSCH model for the high viscosity and low viscosity cases for composition 50%-50% and 30%-70%, respectively. The patterns are very different for the two compositions: composition 50%-50% gives rise to pink macrodomains with a tortuous interface, while from composition 30%-70% one gets many small domains with a more or less elongated shape. Switching from high viscosities to low viscosities in the NSCH model does not produce significant differences in the appearance of the domains until $t = 100$ for composition 50%-50%. Compare center and bottom row in Fig. 6. This is somewhat expected from the fact that the lines corresponding to the two cases in Fig. 4 (left) are almost superimposed until about

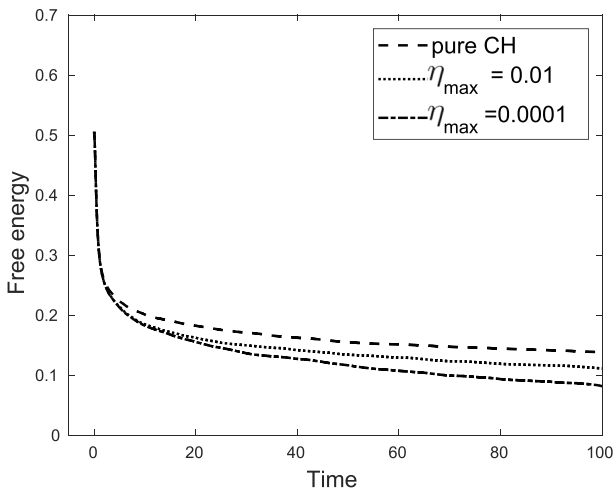


Fig. 5 Average discrete Lyapunov energy (25) given by the CH model and the NSCH model with high values of viscosities ($\eta_1 = 0.01$, $\eta_2 = 0.0008$) and low values of viscosities ($\eta_1 = 0.0001$, $\eta_2 = 0.000008$). The average is taken over ten simulations for composition 30%-70% (right) with different realizations of the random initial distribution

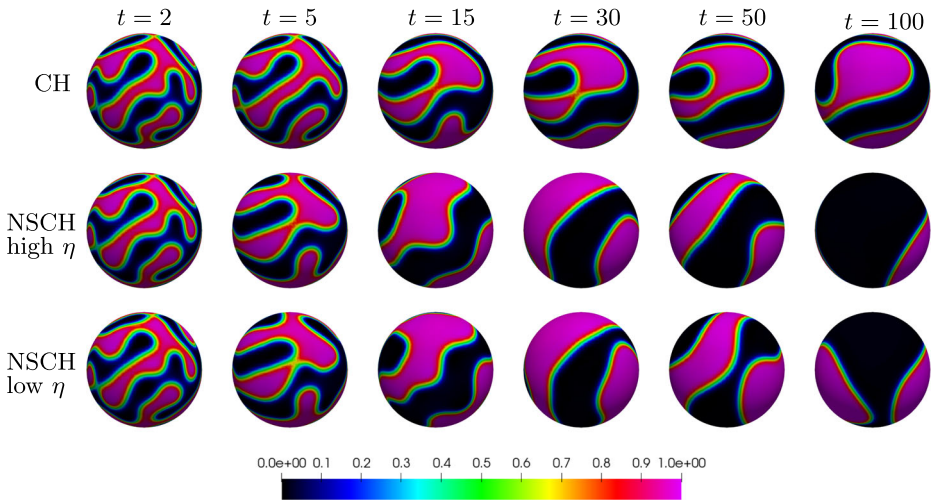


Fig. 6 Phase separation given by the CH model (top), NSCH model with viscosities $\eta_1 = 0.01$, $\eta_2 = 0.0008$ (center), and NSCH model with viscosities $\eta_1 = 0.0001$, $\eta_2 = 0.000008$ (bottom) for composition 50%-50%

$t = 80$. The change in domain appearance happens faster when going from high viscosities to low viscosities for composition 30%-70%. Indeed, by comparing center and bottom row in Fig. 7 we observe remarkable differences already at $t = 40$. Again, this can have been expected from looking at the two lines for the NSCH model in Fig. 4 (right).

Finally, let us take a look at the fluid flow in Figs. 8 and 9 for compositions 50%-50% and 30%-70%, respectively. In both figures, the velocity vectors have been magnified by a factor 5. We see that the velocity magnitude in the bottom row of both figures is larger than

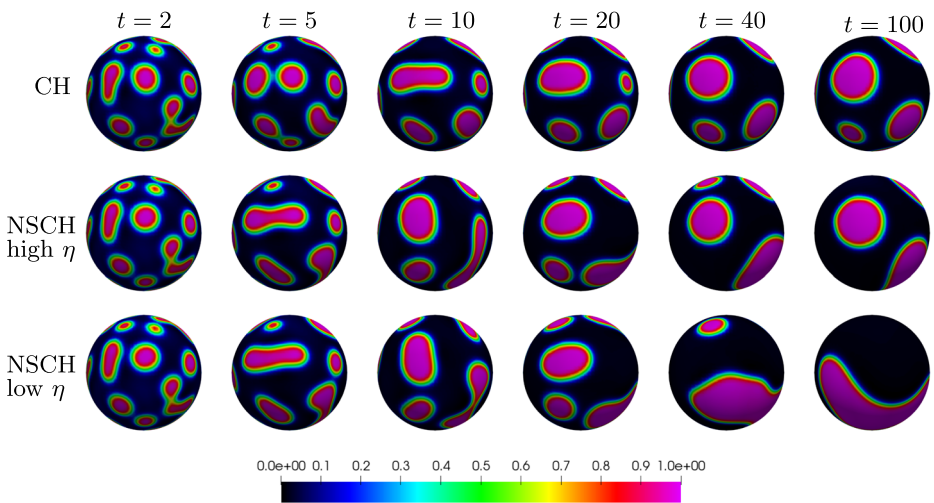


Fig. 7 Phase separation given by the CH model (top), NSCH model with viscosities $\eta_1 = 0.01$, $\eta_2 = 0.0008$ (center), and NSCH model with viscosities $\eta_1 = 0.0001$, $\eta_2 = 0.000008$ (bottom) for composition 30%-70%

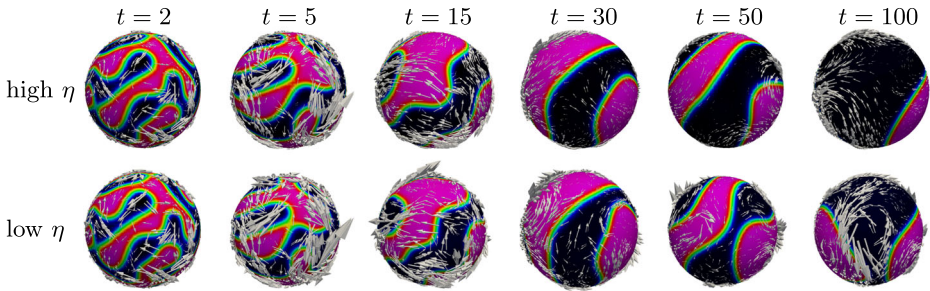


Fig. 8 Velocity vectors superimposed to the surface fraction for $\eta_1 = 10^{-2}, \eta_2 = 8 \cdot 10^{-4}$ (top row) and $\eta_1 = 10^{-4}, \eta_2 = 8 \cdot 10^{-6}$ (bottom row) for composition 50%-50%. For visualization purposes, the velocity vectors are magnified by a factor 5 in both rows

in the top row for every time under consideration, as one would expect when inertial forces become more dominant over viscous forces.

4.2 Phase Separation on a Torus

We consider a more complex surface than the sphere used so far. We choose an asymmetric torus with constant distance from the center of the tube to the origin $R = 1$ and variable radius of the tube: $r_{min} = 0.3 \leq r(x, y) \leq r_{max} = 0.6$, with $r(x, y) = r_{min} + 0.5(r_{max} - r_{min})(1 - \frac{x}{\sqrt{x^2 + y^2}})$. We note that toroidal vesicles are not uncommon [35]. We characterize the torus surface as the zero level set of function $\phi = (x^2 + y^2 + z^2 + R^2 - r(x, y)^2)^2 - 4R^2(x^2 + y^2)$. The torus is embedded in an outer domain $\Omega = [-5/3, 5/3]^3$, just like the sphere. We also selected same mesh level, i.e. $l = 5$.

Like in Section 4.1.1, we focus on composition 50%-50% and select $\rho_1 = 3, \rho_2 = 1$. Line tension is set to $\sigma_\gamma = 0.04$ and we consider that same high viscosity and low viscosity cases as in Section 4.1.2.

Figure 10 reports the discrete Lyapunov energy (25) over time computed by the CH model, NSCH model with low and high viscosities on the torus (left) and sphere (right). Figure 10 (right) is the same as Fig. 4 (left); it is reported again to facilitate the comparison. On the torus, just like on the sphere, the presence of surface flow leads to a faster Lyapunov energy decay. Moreover, on both surfaces switching from high to low values of the viscosity

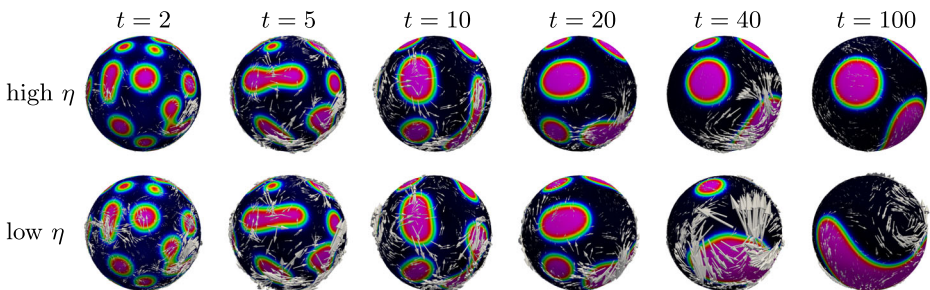


Fig. 9 Velocity vectors superimposed to the surface fraction for $\eta_1 = 10^{-2}, \eta_2 = 8 \cdot 10^{-4}$ (top row) and $\eta_1 = 10^{-4}, \eta_2 = 8 \cdot 10^{-6}$ (bottom row) for composition 30%-70%. For visualization purposes, the velocity vectors are magnified by a factor 5 in both rows

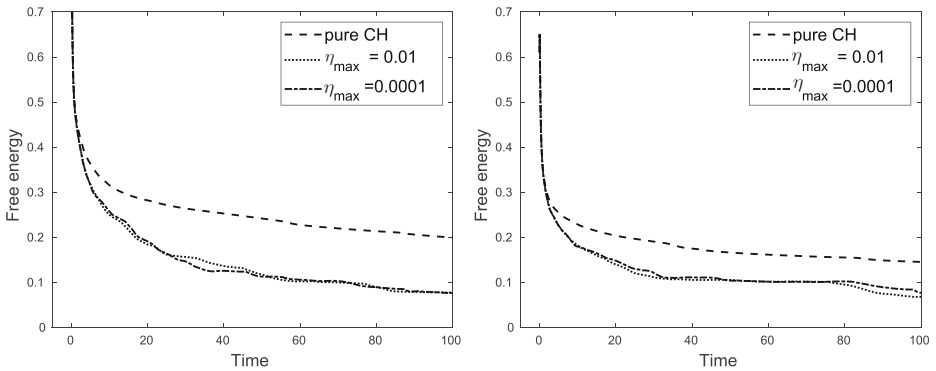


Fig. 10 Discrete Lyapunov energy (25) given by the CH model, NSCH model with high values of viscosities ($\eta_1 = 0.01, \eta_2 = 0.0008$), and NSCH model with low values of viscosities ($\eta_1 = 0.0001, \eta_2 = 0.000008$) on the torus (left) and sphere (right)

does not produce a significant change in the Lyapunov energy decay. On the sphere though, the energy drops to a lower value after the initial fast phase of phase separation and flattens faster in the subsequent slower phase. This suggests an effect of the surface geometry on the evolution of phases.

The effect of the geometry can be seen also when comparing Fig. 6 with Fig. 11, which shows the evolution of phases delivered by the CH model and NSCH model for the high viscosity and low viscosity cases on the torus. We see that the interface separating the two phases remains tortuous for a longer period of time on the torus. As for within the torus itself, we do not observe a particular difference in pattern between “skinny” and “fat” side of the torus.

Next, in Fig. 12 we report the the velocity vectors superimposed to the surface fraction for the bottom two cases in Fig. 11. The velocity vectors have been magnified by a factor

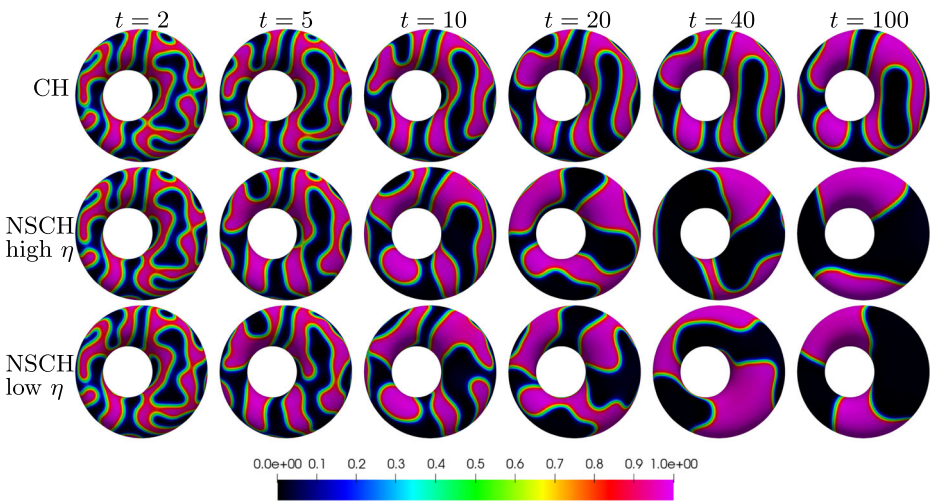


Fig. 11 Phase separation given by the CH model (top), NSCH model with viscosities $\eta_1 = 0.01, \eta_2 = 0.0008$ (center), and NSCH model with viscosities $\eta_1 = 0.0001, \eta_2 = 0.000008$ (bottom)

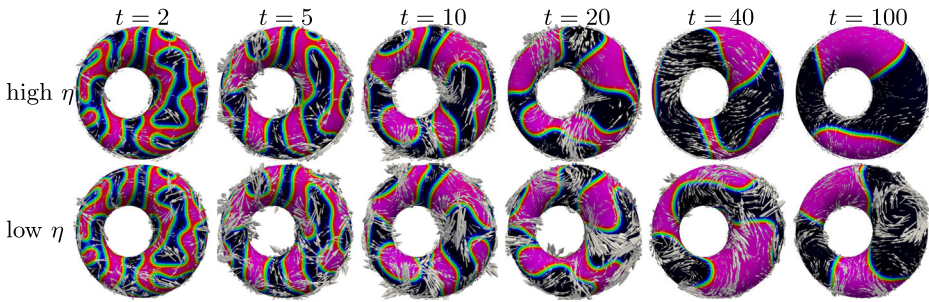


Fig. 12 Velocity vectors superimposed to the surface fraction for $\eta_1 = 10^{-2}$, $\eta_2 = 8 \cdot 10^{-4}$ (top row) and $\eta_1 = 10^{-4}$, $\eta_2 = 8 \cdot 10^{-6}$ (bottom row). For visualization purposes, the velocity vectors are magnified by a factor 5 in both rows

5. This allows us to compare the fluid flows on the sphere (in Fig. 8) and the torus. We observe more intricate flow patterns on the torus due to both the more complex shape and the persistence of the tortuosity in the interface separating the phases.

5 Conclusions

We performed a computational study of lateral phase separation and coarsening on surfaces. To model these processes, we considered both the Cahn–Hilliard (phase separation alone) and the Navier–Stokes–Cahn–Hilliard (phase separation coupled to lateral flow) equations posed on manifolds. Both models were solved numerically using an unfitted finite element method called TraceFEM, which allows for a flexible treatment of complex and evolving surfaces. This choice is motivated by our interest in the computational design of lipid membranes used as drug carriers.

Through a series of numerical tests on the surface of a sphere and an asymmetric torus, we investigated how the evolution of phases changes when switching from the Cahn–Hilliard (CH) model to the Navier–Stokes–Cahn–Hilliard (NSCH) model with variable line tension, viscosity, and membrane composition. We observed that the discrete Lyapunov energy decays faster when using the NSCH model. In particular, such faster decay is more significant when the line tension is increased and the viscosity is lowered. The latter is more evident in some membrane compositions (i.e., 30%–70%) than others (i.e., 50%–50%). Finally, by comparing the evolution of phases on the sphere and on the torus we do observe differences that indicate an effect of the surface geometry.

Acknowledgements This work was partially supported by US National Science Foundation (NSF) through grant DMS-1953535. M.O. also acknowledge the support from NSF through DMS-2011444. A.Q. also acknowledges support from the Radcliffe Institute for Advanced Study at Harvard University where she has been the 2021–2022 William and Flora Hewlett Foundation Fellow.

References

1. Abels, H., Garcke, H., Grün, G.: Thermodynamically consistent, frame in different diffuse interface models for incompressible two-phase flows with different densities. *Math. Models Methods Appl. Sci.* **22**, 1150013 (2012)

2. Abels, H., Breit, D.: Weak solutions for a non-Newtonian diffuse interface model with different densities. *Nonlinearity* **29**, 3426 (2016)
3. Abels, H., Garcke, H., Weber, J.: Existence of weak solutions for a diffuse interface model for two-phase flow with surfactants. *Commun. Pure Appl. Anal.* **18**, 195–225 (2019)
4. Andelman, D., Kawakatsu, T., Kawasaki, K.: Equilibrium shape of two-component unilamellar membranes and vesicles. *EPL Europhys. Lett.* **19**, 57 (1992)
5. Bálint, Š., Dustin, M.L.: Localizing order to boost signaling. *eLife* **6**, e25375 (2017)
6. Bandekar, A., Zhu, C., Gomez, A., Menzenski, M.Z., Sempkowski, M., Sofou, S.: Masking and triggered unmasking of targeting ligands on liposomal chemotherapy selectively suppress tumor growth in vivo. *Mol. Pharm.* **10**, 152–160 (2013)
7. Bartezzaghi, A., Dedè, L., Quarteroni, A.: Isogeometric analysis of high order partial differential equations on surfaces. *Comput. Methods Appl. Mech. Eng.* **295**, 446–469 (2015)
8. Baumgart, T., Hess, S.T., Webb, W.W.: Imaging coexisting fluid domains in biomembrane models coupling curvature and line tension. *Nature* **425**, 821–824 (2003)
9. Bennett, W.F.D., Tieleman, D.P.: Computer simulations of lipid membrane domains. *Biochim. Biophys. Acta (BBA) - Biomembr.* **1828**, 1765–1776 (2013)
10. Cahn, J.W., Hilliard, J.E.: Free energy of a nonuniform system. I. Interfacial Free Energy. *J. Chem. Phys.* **28**, 258–267 (1958)
11. Cahn, J.W.: On spinodal decomposition. *Acta Metall.* **9**, 795–801 (1961)
12. Dedè, L., Quarteroni, A.: Isogeometric analysis of a phase field model for darcy flows with discontinuous data. *Chin. Ann. Math. Ser. B* **39**, 487–512 (2018)
13. DROPS package. <http://www.igpm.rwth-aachen.de/DROPS/>
14. Dziuk, G., Elliott, C.M.: Finite element methods for surface PDEs. *Acta Numer.* **22**, 289–396 (2013)
15. Eilks, C., Elliott, C.M.: Numerical simulation of dealloying by surface dissolution via the evolving surface finite element method. *J. Comput. Phys.* **227**, 9727–9741 (2008)
16. Elliott, C.M., Ranner, T.: Evolving surface finite element method for the Cahn–Hilliard equation. *Numer. Math.* **129**, 483–534 (2015)
17. Funkhouser, C.M., Solis, F.J., Thornton, K.: Dynamics of coarsening in multicomponent lipid vesicles with non-uniform mechanical properties. *J. Chem. Phys.* **140**, 144908 (2014)
18. Gómez, H., Calo, V.M., Bazilevs, Y., Hughes, T.J.: Isogeometric analysis of the Cahn–Hilliard phase-field model. *Comput. Methods Appl. Mech. Eng.* **197**, 4333–4352 (2008)
19. Grande, J., Lehrenfeld, C., Reusken, A.: Analysis of a high-order trace finite element method for PDEs on level set surfaces. *SIAM J. Numer. Anal.* **56**, 228–255 (2018)
20. Gurtin, M.E., Murdoch, A.I.: A continuum theory of elastic material surfaces. *Arch. Rational Mech. Anal.* **57**, 291–323 (1975)
21. Harden, J.L., MacKintosh, F.C.: Shape transformations of domains in mixed-fluid films and bilayer membranes. *EPL Europhys. Lett.* **28**, 495 (1994)
22. Heberle, F.A., Feigenson, G.W.: Phase separation in lipid membranes. *Cold Spring Harb. Perspect. Biol.* **3**, a004630 (2011)
23. Hilliard, J.E.: Spinodal Decomposition. In: Aaronson, H.I. (ed.) *Phase Transformations*, pp. 497–560. American Society for Metals (1970)
24. Hohenberg, P.C., Halperin, B.I.: Theory of dynamic critical phenomena. *Rev. Mod. Phys.* **49**, 435–479 (1977)
25. Jankuhn, T., Olshanskii, M.A., Reusken, A., Zhiliakov, A.: Error analysis of higher order trace finite element methods for the surface Stokes equation. *J. Numer. Math.* **29**, 245–267 (2021)
26. Kahya, N., Scherfeld, D., Bacia, K., Poolman, B., Schwille, P.: Probing lipid mobility of raft-exhibiting model membranes by fluorescence correlation spectroscopy. *J. Biol. Chem.* **278**, 28109–28115 (2003)
27. Kawakatsu, T., Andelman, D., Kawasaki, K., Taniguchi, T.: Phase transitions and shapes of two component membranes and vesicles i: strong segregation limit. *J. Phys. II France* **3**, 971–997 (1993)
28. Kawano, K., Onose, E., Hattori, Y., Maitani, Y.: Higher liposomal membrane fluidity enhances the in vitro antitumor activity of folate-targeted liposomal mitoxantrone. *Mol. Pharm.* **6**, 98–104 (2009)
29. Landau, L.D., Lifshitz, E.M.: *Statistical Physics*. Pergamon, Oxford (1958)
30. Laradji, M., Sunil Kumar, P.B.: Dynamics of domain growth in self-assembled fluid vesicles. *Phys. Rev. Lett.* **93**, 198105 (2004)
31. Levental, I., Levental, K.R., Heberle, F.A.: Lipid rafts: Controversies resolved, mysteries remain. *Trends Cell Biol.* **30**, 341–353 (2020)
32. Li, S., Lowengrub, J., Voigt, A.: Locomotion, wrinkling, and budding of a multicomponent vesicle in viscous fluids. *Commun. Math. Sci.* **10**, 645–670 (2012)
33. Lowengrub, J.S., Rätz, A., Voigt, A.: Phase-field modeling of the dynamics of multicomponent vesicles: Spinodal decomposition, coarsening, budding, and fission. *Phys. Rev. E* **79**, 031926 (2009)

34. Marrink, S.J., Mark, A.E.: Molecular dynamics simulation of the formation, structure, and dynamics of small phospholipid vesicles. *J. Am. Chem. Soc.* **125**, 15233–15242 (2003)
35. Mutz, M., Bensimon, D.: Observation of toroidal vesicles. *Phys. Rev. A* **43**, 4525 (1991)
36. Niemelä, P., Ollila, S., Hyvönen, M., Karttunen, M., Vattulainen, I.: Assessing the nature of lipid raft membranes. *PLoS Comput. Biol.* **3**, e34 (2007)
37. Nitschke, I., Voigt, A., Wensch, J.: A finite element approach to incompressible two-phase flow on manifolds. *J. Fluid Mech.* **708**, 418–7438 (2012)
38. Olshanskii, M.A., Reusken, A., Grande, J.: A finite element method for elliptic equations on surfaces. *SIAM J. Numer. Anal.* **47**, 3339–3358 (2009)
39. Olshanskii, M.A., Xu, X.: A trace finite element method for PDEs on evolving surfaces. *SIAM J. Sci. Comput.* **39**, 1301–1319 (2017)
40. Olshanskii, M.A.: A low order Galerkin finite element method for the Navier–Stokes equations of steady incompressible flow: a stabilization issue and iterative methods. *Comput. Methods Appl. Mech. Eng.* **191**, 5515–5536 (2002)
41. Palzhanov, Y., Zhiliakov, A., Quaini, A., Olshanskii, M.: A decoupled, stable, and linear FEM for a phase-field model of variable density two-phase incompressible surface flow. *Comput. Methods Appl. Mech. Eng.* **387**, 114167 (2021)
42. Seifert, U.: Curvature-induced lateral phase segregation in two-component vesicles. *Phys. Rev. Lett.* **70**, 1335–1338 (1993)
43. Sempkowski, M., Zhu, C., Menzenski, M.Z., Kevrekidis, I.G., Bruchertseifer, F., Morgenstern, A., Sofou, S.: Sticky patches on lipid nanoparticles enable the selective targeting and killing of untargetable cancer cells. *Langmuir* **32**, 8329–8338 (2016)
44. Sezgin, E., Levental, I., Grzybek, M., Schwarzmann, G., Mueller, V., Honigmann, A., Belov, V.N., Eggeling, C., Coskun, Ü., Simons, K., Schwille, P.: Partitioning, diffusion, and ligand binding of raft lipid analogs in model and cellular plasma membranes. *Biochim. Biophys. Acta (BBA) - Biomembr.* **1818**, 1777–1784 (2012)
45. Shen, J., Yang, X.: Numerical approximations of Allen-Cahn and Cahn-Hilliard equations. *Discrete Contin. Dyn. Syst. - A* **28**, 1669–1691 (2010)
46. Sohn, J.S., Tseng, Y.-H., Li, S., Voigt, A., Lowengrub, J.S.: Dynamics of multicomponent vesicles in a viscous fluid. *J. Comput. Phys.* **229**, 119–144 (2010)
47. Stanich, C.A., Honerkamp-Smith, A.R., Putzel, G.G., Warth, C.S., Lamprecht, A.K., Mandal, P., Mann, E., Hua, T.-A.D., Keller, S.L.: Coarsening dynamics of domains in lipid membranes. *Biophys. J.* **105**, 444–454 (2013)
48. Steinbach, I.: Phase-field models in materials science. *Model. Simul. Mater. Sci. Eng.* **17**, 073001 (2009)
49. Veatch, S.L., Keller, S.L.: Separation of liquid phases in giant vesicles of ternary mixtures of phospholipids and cholesterol. *Biophys. J.* **85**, 3074–3083 (2003)
50. Wang, X., Du, Q.: Modelling and simulations of multi-component lipid membranes and open membranes via diffuse interface approaches. *J. Math. Biol.* **56**, 347–371 (2008)
51. Wang, Y., Palzhanov, Y., Quaini, A., Olshanskii, M., Majd, S.: Lipid domain coarsening and fluidity in multicomponent lipid vesicles: a continuum based model and its experimental validation. *Biochim. Biophys. Acta (BBA) - Biomembr.* **1864**, 183898 (2022)
52. Yushutin, V., Quaini, A., Majd, S., Olshanskii, M.: A computational study of lateral phase separation in biological membranes. *Int. J. Numer. Methods Biomed. Eng.* **35**, e3181 (2019)
53. Yushutin, V., Quaini, A., Olshanskii, M.: Numerical modeling of phase separation on dynamic surfaces. *J. Comput. Phys.* **407**, 109126 (2020)
54. Zhiliakov, A., Wang, Y., Quaini, A., Olshanskii, M., Majd, S.: Experimental validation of a phase-field model to predict coarsening dynamics of lipid domains in multicomponent membranes. *Biochim. Biophys. Acta (BBA) - Biomembr.* **1863**, 183446 (2021)